

Tunable phase transitions from semimetals to Chern insulators in two-dimensional quadratic-band-crossing materials

Wen-Hao Bian^{1,2} and Jing Wang^{1,3,*}

¹*Department of Physics, Tianjin University, Tianjin 300072, P.R. China*

²*School of Physics, Nanjing University, Nanjing, Jiangsu 210093, P.R. China*

³*Tianjin Key Laboratory of Low Dimensional Materials Physics and Preparing Technology, Tianjin University, Tianjin 300072, P.R. China*

(Dated: June 25, 2025)

We systematically investigate how static symmetry-breaking perturbations and dynamic Floquet terms via a polarized light manipulate the topological phase transitions in the two-dimensional quadratic-band-crossing-point (QBCP) materials. The Berry curvature shows distinct behavior in such two situations. It is linearly and quadratically proportional to the product of microstructural parameters $t_{x,z}$ for the former and the latter, respectively. The static perturbation eliminates the QBCP and opens an energy gap, which leads to the momentum-inversion symmetry of Berry curvature. This yields a nontrivial Chern number determined by the microstructural parameters. In contrast, we demonstrate that either a circularly or an elliptically polarized light breaks the time-reversal symmetry, transforming the QBCP semimetal into a Chern insulator with a quantized anomalous Hall conductivity $\sigma_{xy} = Ce^2/\hbar$, where the Chern number is governed by the polarization angle. Moreover, the linear polarization preserves the central antisymmetry of the Berry curvature, giving rise to a topological trivial insulator. These results establish a tunable topological phase transition from a QBCP semimetal to Chern insulator in the two-dimensional QBCP materials.

I. Introduction

Topological insulators (TIs) are one of the most important and hottest topics in contemporary condensed matter physics, which fundamentally differ from conventional band insulators by exhibiting both insulating bulk states and topologically protected metallic edge/surface states [1–5]. These unique properties have been attracting a plethora of both experimental and theoretical studies [2–14]. Whether the time-reversal symmetry (TRS) is preserved or broken gives rise to two distinct categories of TIs in two dimensions. One is the \mathbb{Z}_2 topological insulator protected by the TRS and characterized the \mathbb{Z}_2 index [2, 15]. On the contrary, the other corresponds to the Chern insulator that breaks the TRS and is characterized by a nontrivial Chern number and non-zero anomalous Hall conductivity (AHC) [1, 16]. Especially, Chern insulators have become a crucial research frontier in topological quantum materials. Beyond the

Haldane model [1], both the higher-order Chern insulators [17, 18] and dual Chern insulators have been proposed [19]. Besides, several groups [1, 16–27] recently advocate the fractional Chern insulators which host fractionalized excitations. Since the quantum anomalous Hall effect in Chern insulator was observed in $\text{Cr}_{0.15}(\text{Bi}_{0.1}\text{Sb}_{0.9})_{1.85}\text{Te}_3$ [26], the experimental studies on Chern insulators also made significant progress including quantum computing [20], topological state manipulation [20, 27], and quantum simulation [28–30].

Particularly, topological phase transitions have garnered extensive studies in various kinds of semimetals, including Dirac semimetals characterized by linear dispersions [15, 31–38] and semi-Dirac materials equipped with hybrid linear-quadratic dispersions [39–43]. In recent years, attention has gradually shifted to a new type of semimetal. Considering this type of semimetal, upper and lower bands parabolically touching at a quadratic band crossing point (QBCP) [44–49]. The quadratic dispersion in such systems leads to an enhanced density of states and gives rise to unique symmetry-protected

* Corresponding author: jing.wang@tju.edu.cn

topological properties that are absent in their linear counterparts [44, 46, 47, 50–55]. Additionally, certain interaction-driven topological phase transitions in these materials have been reported [50–53, 56–58]. While the perturbation control of topological phases was advocated in Dirac systems [38, 40, 59], its application to the QBCP semimetals, however, has not yet been sufficiently investigated. Especially, there exist two important issues to be delved into. Initially, it is worth examining how static and dynamic perturbations induced by tunable external optical fields distinctively influence the topological properties of QBCP systems. Besides, it is imperative to explore the potential of these external optical fields serve as a suitable tool to control the topological phase transitions between trivial and nontrivial phases.

To this end, we systematically investigate the effects of static perturbations and tunable optical fields as well as their interplay on the the topological properties of 2D QBCP semimetals. Specifically, we begin with the study of a static perturbation. It generates opens an energy gap with breaking TRS and causes the Berry curvature symmetric under momentum inversion, yielding Chern insulators with nontrivial quantized Chern numbers $C = \pm \text{sgn}(t_x t_z)$ governed by structural parameters. Next, a polarized light irradiation is imposed on the QBCP system by adopting the Floquet theory [60–64]. We find that either a circularly or an elliptically tunable polarized light breaks the TRS, transforming the QBCP semimetal into a Chern insulator with $C = \pm \text{sgn}(\phi)$. In comparison, the linear polarization preserves trivial topology. Hereby, the polarization angle (ϕ) acts as a tunable parameter to switch a trivial and Chern insulator. Furthermore, we briefly examine the competition between static and dynamically optical perturbations, which measured by the parameters m and A_0 , respectively. At $m \gg A_0$, the former dominates with $C = \pm \text{sgn}(t_x t_z)$, whereas $A_0 \gg m$ enables the latter become dominant. At last, the behavior of AHC accompanied by the topological phase transitions at zero temperature is addressed. Both types of perturbations exhibit a universal quantization $\sigma_{xy} = Ce^2/\hbar$ with $C = 1$ at the Fermi energy but instead present non-universal scalings

in other regimes that are modulated by the parameters t_I and A_0/ϕ for static and dynamic perturbations, respectively. These results resolve the interplay between symmetry constraints, geometric Berry response, and topological phase transitions in QBCP materials, providing theoretical references for further studies of the related quantum materials.

The rest of this paper is organized as follows. In Sec. II, we present three effective models, including the free QBCP model, perturbative model, and Floquet model, to construct the effective Hamiltonian. Subsequently, Sec. III is followed to compute the Berry curvature and Chern number, and perform a detailed analysis of the topological phase transitions as well as provide the overall phase diagrams. Thereafter, we within Sec. IV calculate the anomalous Hall conductivity arising from TRSB and nontrivial Berry curvature. Finally, Sec. V concludes with a brief summary of the key results.

II. Effective models

To systematically investigate the topological properties of 2D QBCP semimetals, we within this work consider three distinct models, which are denominated as the free model that preserves both C_4 point-group symmetry and TRS [45–48], the perturbative model incorporating an external field to break TRS [40, 44], and the Floquet model with a time-periodic driving [40, 60–68], respectively.

A. Free model

At first, let us introduce the free model. The free effective continuous Hamiltonian for 2D QBCP semimetals with a checkerboard lattice is given by [45–48]

$$H_0 = \sum_{\sigma=\uparrow\downarrow} \sum_{\mathbf{k}<|\Lambda|} \Psi_{\mathbf{k}\sigma}^\dagger \mathcal{H}_0(\mathbf{k}) \Psi_{\mathbf{k}\sigma}, \quad (1)$$

where Λ serves as the momentum cutoff associated with the lattice constant, and $\Psi_{\mathbf{k}\sigma} = (c_{a\sigma}, c_{b\sigma})^T$ represents the sublattice spinor with the indexes a and b denoting sublattices and σ being the spin of electron. The

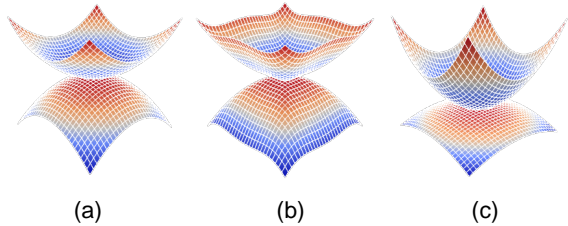


FIG. 1. (Color online) Schematic dispersions for the 2D QBCP semimetals: (a) $t_x = t_z$, (b) $t_x \neq t_z$ with $t_I = 0$, and (c) $t_x = t_z$ with $t_I \neq 0$.

Hamiltonian density takes the form:

$$\mathcal{H}_0(\mathbf{k}) = t_I \mathbf{k}^2 \sigma_0 + 2t_x k_x k_y \sigma_1 + t_z (k_x^2 - k_y^2) \sigma_3. \quad (2)$$

Hereby, t_I , t_x , and t_z correspond to material-dependent parameters and the Pauli matrices $\sigma_{1,2,3}$ with the identity matrix σ_0 act on the sublattice space. The Hamiltonian density can also be written compactly as

$$\mathcal{H}_0 = t_I \mathbf{k}^2 \sigma_0 + \mathbf{d}_0(\mathbf{k}) \cdot \boldsymbol{\sigma}, \quad (3)$$

with $\mathbf{d}_0(\mathbf{k}) = (2t_x k_x k_y, 0, t_z (k_x^2 - k_y^2))$.

Diagonalizing $\mathcal{H}_0(\mathbf{k})$ yields the parabolical energy eigenvalues [45–49, 69],

$$E_{\mathbf{k}}^{\pm} = \frac{\mathbf{k}^2 \left(\lambda \pm \sqrt{\cos^2 \eta \cos^2 2\theta_{\mathbf{k}} + \sin^2 \eta \sin^2 2\theta_{\mathbf{k}}} \right)}{\sqrt{2}m}, \quad (4)$$

where

$$m = \frac{1}{\sqrt{2(t_x^2 + t_z^2)}}, \lambda = \frac{t_I}{\sqrt{t_x^2 + t_z^2}}, \quad (5)$$

$$\cos \eta = \frac{t_z}{\sqrt{t_x^2 + t_z^2}}, \sin \eta = \frac{t_x}{\sqrt{t_x^2 + t_z^2}}, \quad (6)$$

$$\cos \theta_{\mathbf{k}} = \frac{k_x}{\sqrt{k_x^2 + k_y^2}}, \sin \theta_{\mathbf{k}} = \frac{k_y}{\sqrt{k_x^2 + k_y^2}}, \quad (7)$$

with $\theta_{\mathbf{k}}$ specifying the direction of momentum. This energy dispersion features two bands: an upper band and a lower band, which touch quadratically at a quadratic band crossing point (QBCP) with $\mathbf{k} = 0$ when the condition $|t_I| < \min(|t_x|, |t_z|)$ is satisfied. It is of particular importance to highlight that the particle-hole (PH) and rotational symmetries depend upon the microstructural parameters as schematically depicted in Fig. 1.

A nonzero parameter t_I explicitly breaks the PH symmetry, and the rotational symmetry is preserved when $t_x = t_z$ but broken otherwise.

In particular, the 2D QBCP free Hamiltonian (2) exhibits two fundamental symmetries. Specifically, it satisfies the time-reversal symmetry (TRS) under $\mathcal{T}\mathcal{H}_0(\mathbf{k})\mathcal{T}^{-1} = \mathcal{H}_0(-\mathbf{k})$ due to a paucity of σ_2 term [46, 47]. Besides, the Hamiltonian respects the spatial inversion symmetry expressed as $\mathcal{P}\mathcal{H}_0(\mathbf{k})\mathcal{P}^{-1} = \mathcal{H}_0(-\mathbf{k})$. Herein, \mathcal{T} and \mathcal{P} are the time-reversal and parity operators, respectively.

The σ_1 and σ_3 terms in the free Hamiltonian (2) originate from the symmetries of the d_{xy} - and $d_{x^2-y^2}$ -orbital wavefunctions. These terms give rise to a net Berry flux of $\pm 2\pi$ around the QBCP [46, 47]. This accordingly indicates that the free Hamiltonian (2) describes a robust semimetal state that hosts a QBCP at $\mathbf{k} = 0$ and is protected by TRS. A critical question then arises: Can the system exhibit topologically nontrivial states if the QBCP is removed or if TRS is explicitly broken? To address this, we propose two strategies for realizing time-reversal symmetry breaking (TRSB), which will be detailed in Sec. II B.

B. Perturbative and Floquet models

Next, we bring out the other two models. To enable certain topological phase transition and induce nontrivial topological properties in the 2D QBCP system, it is essential to breaking TRS [3–5, 7]. To this end, we bring out two distinct approaches: (a) introducing a generic perturbation term to the free model (2), and (b) employing the light-matter interaction as a realistic symmetry-breaking mechanism.

1. Perturbation model

As a simple toy model and control case, let us begin with removing the QBCP and opening an energy gap via the introduction of a perturbation constant term $\delta\mathcal{H}$, which can be realized by interactions, impurities, periodic potentials, etc. [13, 40, 70–73]. Then the free

model (2) is casted into [39, 40, 73]

$$\mathcal{H}_{\text{pert}}(\mathbf{k}) = \mathcal{H}_0(\mathbf{k}) + \delta\mathcal{H}, \quad (8)$$

we highlight that the perturbation term $\delta\mathcal{H}$ is not arbitrarily chosen [44, 74].

When we consider $\delta\mathcal{H} = m_i\sigma_i$ with $i = 1, 3$, the QBCP cannot be removed but splitting into two distinct quadratic touching points as shown in Fig. 2. For $m_1 \neq 0, m_3 = 0$, the QBCP splits into two points at $\mathbf{k} = \sqrt{m_1/2t_x}(\pm 1, \mp 1)$ ($m_1 t_x > 0$) or $\mathbf{k} = \sqrt{-m_1/2t_x}(\pm 1, \pm 1)$ ($m_1 t_x < 0$), aligned with $k_x = \pm k_y$. For $m_1 = 0, m_3 \neq 0$, the points shift to $k_y = 0$ ($m_3 > 0$) or $k_x = 0$ ($m_3 < 0$). In the general case ($m_1, m_3 \neq 0$), the points locate at $\mathbf{k} = (\pm\sqrt{\alpha/2}, \mp m_1/(t_x\sqrt{2\alpha}))$ with $\alpha = -m_3/t_z + \sqrt{(m_3/t_z)^2 + (m_1/t_x)^2}$ [44].

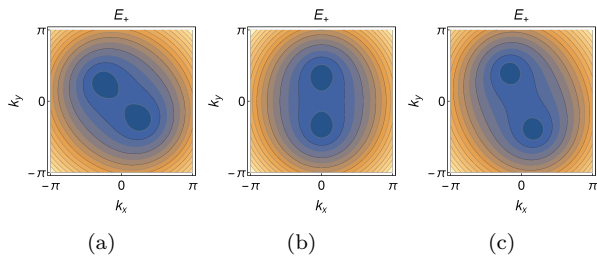


FIG. 2. (Color online) Splitting of the quadratic touching points under the perturbative term $\delta\mathcal{H} = m_i\sigma_i$ with $i = 1, 3$: (a) $m_1 \neq 0, m_3 = 0$, (b) $m_3 \neq 0, m_1 = 0$, and (c) $m_1 = m_3 \neq 0$.

In consequence, we are left with $\delta\mathcal{H} = m\sigma_2$ with $m > 0$ as a symmetry-breaking perturbation. The total Hamiltonian dubbed the perturbative model becomes

$$\mathcal{H}_{\text{pert}}(\mathbf{k}) = t_I \mathbf{k}^2 \sigma_0 + \mathbf{h}(\mathbf{k}) \cdot \boldsymbol{\sigma}, \quad (9)$$

with $\mathbf{h}(\mathbf{k}) = (2t_x k_x k_y, m, t_z(k_x^2 - k_y^2))$. The σ_2 perturbation term induces critical effects. The QBCP is elim-

inated and a direct energy gap $\Delta = 2m$ emerges at $\mathbf{k} = \mathbf{0}$. More importantly, the TRS is explicitly broken, namely $\mathcal{T}\mathcal{H}_{\text{per}}(\mathbf{k})\mathcal{T}^{-1} \neq \mathcal{H}_{\text{per}}(-\mathbf{k})$, which are expected to generate non-trivial Berry curvature and nontrivial topological properties [3–5, 7, 40].

2. Floquet model

In order to bridge theoretical model with experiment, we go beyond the toy model presented in Sec. II B 1 and employ light-matter interaction as a realistic symmetry-breaking mechanism, i.e., the Floquet theory [40, 60–68].

Within the Floquet framework, circularly polarized light irradiation provides a controlled pathway to dynamically break TRS without static lattice alterations [40, 60–68, 75–77]. Specifically, the time-periodic modulation is implemented by coupling the Hamiltonian of free model (2) to a monochromatic radiation field $\mathbf{A}(t) = (A_x, A_y) = A_0(\sin(\omega t), \sin(\omega t + \phi))$ where the spatial dependence is neglected as the wavelength of the field is much larger compared to the sample size. Hereby, ω and A_0 denote the frequency and amplitude of the driving field, respectively. The polarization state of light is parameterized by the phase angle $\phi \in (-\pi, \pi]$, which determines the relative phase between orthogonal components of the electric field. This yields three distinct polarization types: the circular polarization (CPL) at $\phi = \pm\pi/2$, the linear polarization (LPL) at $\phi = 0, \pi$, and the elliptical polarization (EPL) for all other values of ϕ . Performing the minimum coupling via $\mathbf{k} \rightarrow \mathbf{k} + e\mathbf{A}(t)$ with e being the electric charge gives rise to the new Hamiltonian [40],

$$\mathcal{H}(\mathbf{k}, t) = \mathcal{H}_0(\mathbf{k}) + H_1\sigma_0 + H_2\sigma_1 + H_3\sigma_3 \quad (10)$$

where

$$H_1 = t_I e A_0 \{ 2k_x \sin(\omega t) + e A_0 \sin^2(\omega t) + \sin(\omega t + \phi) [2k_y + e A_0 \sin(\omega t + \phi)] \}, \quad (11)$$

$$H_2 = 2t_x e A_0 \{ k_x \sin(\omega t + \phi) + \sin(\omega t) [k_y + e A_0 \sin(\omega t + \phi)] \}, \quad (12)$$

$$H_3 = \frac{t_z e A_0}{2} \{ -e A_0 \cos(2\omega t) + e A_0 \cos(2\omega t + 2\phi) + 4k_x \sin(\omega t) - 4k_y \sin(\omega t + \phi) \}. \quad (13)$$

In the spirit of Floquet theory [40, 60–68], the stro-

boscopic dynamics of the time-periodic Hamiltonian

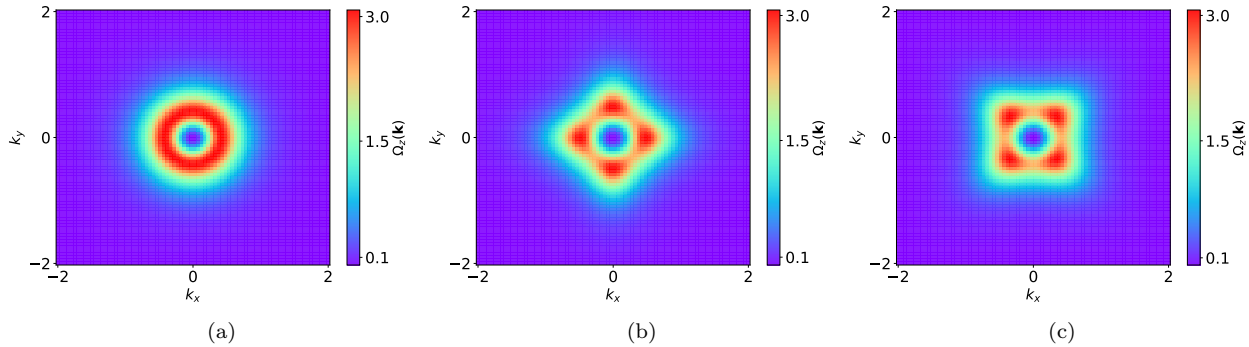


FIG. 3. (Color online) Momentum-dependence Berry curvature for the perturbation model: (a) $t_x = t_z = 1.6$, (b) $t_x = 1.6$, $t_z = 1.2$, (c) $t_x = 1.2$, $t_z = 1.6$ with $m = 0.4$.

can be mapped to an effective static Floquet Hamiltonian $\mathcal{H}_F(\mathbf{k})$. This Floquet Hamiltonian formally satisfies [40, 60–68]

$$\mathcal{H}_F(\mathbf{k}) = \frac{i}{\hbar T} \ln [\mathbf{U}(t_0 + T, t_0)], \quad (14)$$

where $\mathbf{U}(t, t_0) = \mathcal{T}_t \exp \left[-\frac{i}{\hbar} \int_{t_0}^t dt' \mathcal{H}(\mathbf{k}, t') \right]$ is the evolution operator with \mathcal{T}_t denoting the time-ordering operator and t_0 the initial time of the perturbation [40, 65–67]. After several analytical calculations in Ap-

pendix. A, we finally arrive at the effective Hamiltonian of the Floquet model

$$\mathcal{H}_F(\mathbf{k}) = t_I (e^2 A_0^2 + \mathbf{k}^2) \sigma_0 + \mathbf{d}(\mathbf{k}) \cdot \boldsymbol{\sigma}, \quad (15)$$

where the vector takes the form of

$$\mathbf{d}(\mathbf{k}) = (t_x e^2 A_0^2 \cos \phi + 2t_x k_x k_y, m_{\text{eff}}, t_z (k_x^2 - k_y^2)), \quad (16)$$

with the effective mass term depending on the momentum \mathbf{k} and the strength of field \mathbf{A} ,

$$m_{\text{eff}} = \frac{eA_0 t_x t_z}{4\omega \hbar} \left\{ 8e^2 A_0^2 [1 + \cos(2\phi)] k_y + 20eA_0 \sin \phi k_x^2 + 12eA_0 \sin \phi k_y^2 + 4eA_0 \sin(2\phi) k_x k_y - 16e^2 A_0^2 \cos \phi k_x + 16(\cos \phi k_x - k_y) \mathbf{k}^2 + e^3 A_0^3 [3 \sin \phi + \sin(3\phi)] \right\}. \quad (17)$$

The Floquet Hamiltonian in Eq. (15) induces a band gap analogous to the static perturbation model in Sec. II B 1. This gap Δ emerges near $\mathbf{k} \rightarrow \mathbf{0}$ and depends on t_x , t_z , driving amplitude A_0 , polarization angle ϕ , and frequency ω :

$$\Delta = \sqrt{(\delta_1 \cos \phi)^2 + \frac{1}{4} [\delta_2 (3 \sin \phi + \sin(3\phi))]^2}, \quad (18)$$

where ϕ plays a crucial role in the magnitude of gap, and the $\delta_1 = 2t_x e^2 A_0^2$ and $\delta_2 = \frac{e^4 A_0^4 t_x t_z}{\hbar \omega}$ correspond to the gap for LPL ($\phi = 0, \pi$) and CPL ($\phi = \pm\pi/2$), respectively.

On the basis of these models, we are going to address the questions raised in the end of Sec. II A via care-

fully studying the topological nontrivial properties for both perturbative and Floquet models. The resulting topological properties—including Berry curvature, Chern numbers, and anomalous Hall conductivity—will be systematically analyzed in Sec. III and Sec. IV.

III. Berry curvature and Chern number

Within this section, we systematically investigate the Berry curvature, Chern number, and potential topological phase transitions for the effective models established in Sec. II. A generic two-level Hamiltonian can be comprehensively described by [3–5] $\mathcal{H}_0(\mathbf{k}) =$

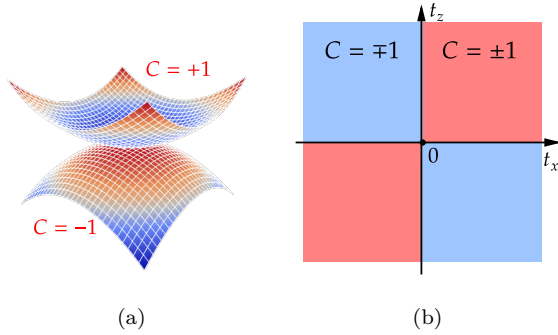


FIG. 4. (Color online) Schematic descriptions of the basic results for the perturbative model: (a) non-trivial Chern numbers of the upper and lower bands and (b) t_x, t_z -tuned topological phase transitions.

$d_0(\mathbf{k})\sigma_0 + \mathbf{d}(\mathbf{k}) \cdot \boldsymbol{\sigma}$ where $d_0(\mathbf{k})$ represents a scalar function of momentum, while $\mathbf{d}(\mathbf{k})$ constitutes a momentum-dependent vector parameter. The former can induce an energy shift of both bands while preserving their relative separation and curvature. In contrast, the latter governs the nontrivial eigenstate geometry that determines all topological characteristics.

A. Perturbative model

As a warm-up, let us consider the perturbative model. Reading from its Hamiltonian (9), the vector field $\mathbf{h}(\mathbf{k})$ takes the form of

$$\mathbf{h}(\mathbf{k}) = (2t_x k_x k_y, m, t_z(k_x^2 - k_y^2)). \quad (19)$$

The Berry curvature that is exclusively polarized along the z -axis for such two-dimensional model can be written as [40, 78, 79].

$$\Omega_z(\mathbf{k}) = \frac{1}{2|\mathbf{h}|^3} \mathbf{h} \cdot (\partial_{k_x} \mathbf{h} \times \partial_{k_y} \mathbf{h}), \quad (20)$$

where $\partial_{k_x} \mathbf{h} \times \partial_{k_y} \mathbf{h}$ encodes the local geometric curvature of the $\mathbf{h}(\mathbf{k})$ on the momentum-space manifold. Substituting the explicit form of $\mathbf{h}(\mathbf{k})$ (19), the Berry curvature simplifies to

$$\Omega_z(\mathbf{k}) = \frac{4t_x t_z m \mathbf{k}^2}{2|\mathbf{h}|^3}, \quad (21)$$

with $|\mathbf{h}| = \pm \sqrt{(2t_x k_x k_y)^2 + m^2 + t_z^2(k_x^2 - k_y^2)^2}$.

This implies that the Berry curvature is symmetric under momentum inversion ($\mathbf{k} \rightarrow -\mathbf{k}$) and invariant under exchange $k_x \leftrightarrow k_y$. In addition, its magnitude is proportional to the product of three parameters $t_x t_z m$. While m modulates the band magnitude, it does not alter the topological properties. Since the rotational symmetry of the system is governed by the ratio t_x/t_z , this indicates the full rotational symmetry is preserved symmetric at ($t_x = t_z$) as displayed in Fig. 3(a), but instead Fig. 3(b)–(c) show the rotational symmetry broken for ($t_x \neq t_z$). In particular, the curvature vanishes at $t_x t_z = 0$, signaling the loss of nontrivial geometry. As long as $t_x t_z$ is nonzero, the Berry curvature remains finite and undergoes reversal under the sign inversion of $t_x t_z$.

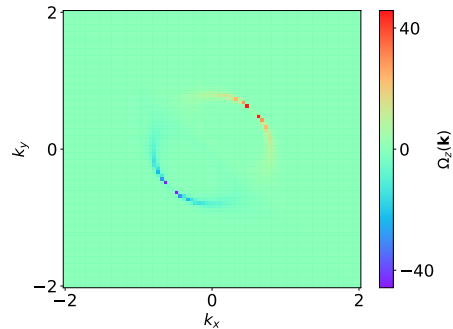


FIG. 5. (Color online) Berry curvature of Floquet model for the LPL at $\phi = \pi$ and $A_0 = 0.8$, $\hbar\omega = 0.43$ with $t_x = t_z = 1.4$.

In order to further investigate the potential topological properties, we need to compute the corresponding Chern number, which is designated by the integral of the Berry curvature over the Brillouin zone (BZ) [3, 4, 40, 78–81]. It is then formulated as

$$C = \frac{1}{2\pi} \int_{\text{BZ}} d^2\mathbf{k} \frac{4t_x t_z m \mathbf{k}^2}{2|\mathbf{h}|^3}. \quad (22)$$

As the Berry curvature of the perturbative model (21) is invariant under momentum inversion, $\Omega_z(\mathbf{k}) = \Omega_z(-\mathbf{k})$, generally supporting a non-trivial Chern number. Indeed, Eq. (22) yields

$$C = \pm \text{sgn}(t_x t_z), \quad (23)$$

where the sign corresponds to the upper and lower bands shown in Fig. 4(a), respectively.

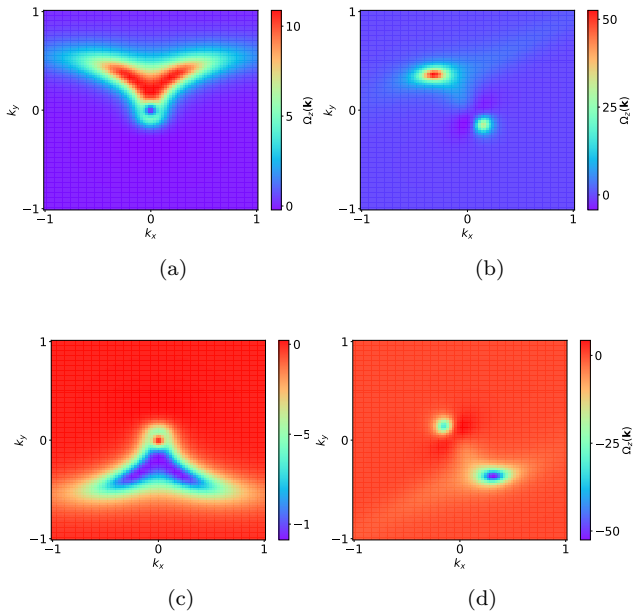


FIG. 6. (Color online) Berry curvature of Floquet model for the RHPL: (a) $\phi = \pi/2$ (CPL) and (b) $\phi = \pi/3$ (EPL), as well as the LHPL: (c) $\phi = -\pi/2$ (CPL) and (d) $\phi = -\pi/3$ (EPL) with $A_0 = 0.43$, $\hbar\omega = 0.8$ and $t_x = 1.4$, $t_z = 2.0$.

This manifestly signifies the perturbative gap transforms a topological transition from the perturbative

$$\Omega_z(\mathbf{k}) = \frac{-1}{2|\mathbf{d}|^3} 2t_x t_z \left[\mathbf{k}^2 (k_x \partial_{k_x} m_{\text{eff}} + k_y \partial_{k_y} m_{\text{eff}} - 2m_{\text{eff}}) + e^2 A_0^2 (k_y \partial_{k_x} m_{\text{eff}} + k_x \partial_{k_y} m_{\text{eff}}) \cos \phi \right]. \quad (24)$$

where \mathbf{d} is designated in Eq. (16). It can be observed that the Berry curvature $\Omega(\mathbf{k})$ explicitly depends on both the microscopic parameters $t_{x,z}$ and the characteristics of the applied electric field including its amplitude A_0 , frequency $\hbar\omega$, and polarization angle ϕ .

Reading off Eq. (24), it can be found that the polarization angle ϕ is crucial to modulate the Berry curvature by controlling the multitude of the second term, which scales as $\cos \phi$. To systematically address this issue, let us consider all three distinct polarization states mentioned in Sec. II B 2.

With respect to the LPL at $\phi = 0, \pi$ displayed in Fig. 5, it considerably suppresses the Berry curvature but preserves the central symmetry about $\mathbf{k} = 0$,

QBCP semimetal to a Chern insulator. Such a quantized result reflects the unique feature of quadratic momentum dependence of the dispersion. In sharp contrast, the semi-Dirac semimetal with the perturbation term still remains a topological trivial state ($C = 0$) [39, 40]. Besides, since the microscopic parameters t_x and t_z illustrated in Fig. 3 govern both the rotational symmetry of the energy bands and the spatial distribution of the Berry curvature, the result (23) implies that continuous parameter variations can drive distinct topological phase transitions. A schematic of this dependence is provided in Fig. 4(b).

As a consequence, it demonstrates that TRSB via a σ_2 -type perturbation in a 2D QBCP semimetal can induce a topological phase transition characterized by a non-zero Chern number.

B. Floquet model

Next, let us consider the underlying topological non-trivial properties for the Floquet model. By utilizing the the vector field (16) and paralleling the similar derivations of the perturbative model, we arrive at the Berry curvature for the Floquet model,

namely $\Omega_z(k_x, k_y) = -\Omega_z(-k_x, -k_y)$. As for the CPL and EPL, we firstly consider the right-handed polarized light (RHPL) in which the ϕ is restricted to $(0, \pi)$. Considering the CPL with $\phi = \pi/2$, the second term in Eq. (24) vanishes. This indicates that the Berry curvature possesses the mirror symmetry about the k_x -axis, i.e., $\Omega_z(k_x) = \Omega_z(-k_x)$, while breaking rotational and k_y -mirror symmetries as depicted in Fig. 6(a). Turning to the EPL, Fig. 6(b) presents the behavior of $\Omega_z(k_x, k_y)$ at as a representative value of $\phi = \pi/3$ (the basic result is similar for other values). Compared to its CPL counterpart, one can notice from Fig. 6(b) that the EPL induces complete symmetry breaking in momentum space: $\Omega_z(k_x, k_y) \neq \Omega_z(-k_x, k_y) \neq \Omega_z(k_x, -k_y)$. In addition,

we have also examined the left-handed polarized light (LHPL) with ϕ located at $(-\pi, 0)$. Fig. 6(c)-(d) suggest that the LHPL shares the analogous results with RHPL but only satisfies $\Omega_z^{\text{LHPL}}(\mathbf{k}) = -\Omega_z^{\text{RHPL}}(\mathbf{k})$ for both CPL and EPL.

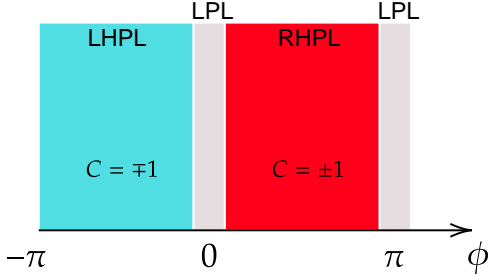


FIG. 7. (Color online) The polarization position ϕ -dependent Chern numbers for the Floquet model. Hereby, the LPL corresponds to topologically trivial state with $C = 0$.

In addition to the polarization angle, we find that the qualitative behavior of Berry curvature exhibits weak dependence on other parameters in Eq. (24) such as the light intensity A_0 , its frequency $\hbar\omega$, and the microscopic structural parameters t_x , t_z . The essential reason is that these parameters can only primarily modulate the magnitude of energy gap but are not able to alter either the topological invariants or symmetry constraints. Particularly, the Berry curvature of the Floquet model (24) scales as $\Omega_z \propto (t_x t_z)^2$ rendering it invariant under sign reversals of t_x or t_z , which is qualitatively different from its counterpart of the perturbative model (21).

To proceed, we are able to discuss the Chern number. As the qualitative behavior of Berry curvature is insensitive to the parameters A_0 , $\hbar\omega$, and t_x, t_z in Eq. (24), they do not alter the topological invariants and cannot influence the topological phase transition. However, the LPL at $\phi = 0, \pi$ causes $\Omega_z(\mathbf{k}) = -\Omega_z(-\mathbf{k})$ and thus yields a trivial Chern number $C = 0$. This signals that the LPL opens an energy gap in the 2D QBCP system, leaving the system in a conventional insulating phase.

In sharp contrast, the application of non-linear polarization (non-LPL, i.e., CPL or EPL) with $\phi \neq 0, \pi$ fundamentally alters the symmetry of Berry curvature, resulting in $\Omega_z(\mathbf{k}) \neq -\Omega_z(-\mathbf{k})$. Paralleling the strategy

in Sec. III A, we find that non-LPL irradiation not only removes the QBCP by opening a energy gap but also induce a topological insulator state, which owns non-trivial Chern numbers $C = \pm 1$ with the sign denoting the upper and lower bands, respectively.

Specifically, the polarization direction (PD) of the light directly governs the sign of the Berry curvature and henceforth determines the Chern number inversion between distinct energy bands: RHPL with $0 < \phi < \pi$ (CPL or EPL) causing a positive Berry curvature $\Omega_z > 0$ and leading to $C = 1$ to the upper band, and its LHPL counterpart ($-\pi < \phi < 0$) giving rise to a negative Berry curvature and the Chern number $C = -1$ for the upper band. This implies that the system undergoes $C_{\text{upper}} \xrightarrow{\phi: 0 \rightarrow -\pi} 1 \rightarrow -1$, $C_{\text{lower}} \xrightarrow{\phi: 0 \rightarrow -\pi} -1 \rightarrow 1$ with tuning the parameter ϕ from RHPL to LHPL. In other words, the sign of PD $\text{sgn}(\phi)$ acts as a tunable order parameter to control a topological phase transition between different topological invariants as schematically shown in Fig. 7.

To wrap up, an irradiation of a 2D QBCP semimetal with a polarization tunable light can open an energy gap and break time-reversal symmetry (TRS), thereby inducing nontrivial and topological properties as summarized in Table I. In particular, a potential topological phase transition can be induced between a Chern insulator and trivial insulator with variation of the PD as displayed in Fig. 7.

TABLE I. Collections of Chern number for the Floquet model under distinct polarization directions (PDs).

	LPL	CPL	EPL	PDs
Chern number	0	± 1	± 1	RHPL
Chern number	0	∓ 1	∓ 1	LHPL

C. Hybrid situation

For completeness, let us study the hybrid situation in which it is irradiated by a polarization light imposed in the Floquet model (15) on the perturbative model (9). In this circumstance, the Berry curvature is reformulated as

$$\Omega_z(\mathbf{k}) = \frac{-1}{2|\mathbf{d}|^3} 2t_x t_z [\mathbf{k}^2 (k_x \partial_{k_x} m_{\text{eff}} + k_y \partial_{k_y} m_{\text{eff}} - 2m_{\text{eff}} - 2m) + e^2 A_0^2 (k_y \partial_{k_x} m_{\text{eff}} + k_x \partial_{k_y} m_{\text{eff}}) \cos \phi], \quad (25)$$

where the magnitude of vector field is designated as

$$|\mathbf{d}(\mathbf{k})| = \pm \sqrt{(t_x e^2 A_0^2 \cos \phi + 2t_x k_x k_y)^2 + (m_{\text{eff}} + m)^2 + t_z^2 (k_x^2 - k_y^2)^2}. \quad (26)$$

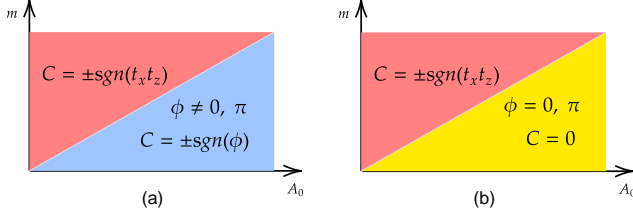


FIG. 8. (Color online) Schematic $m - A_0$ dependent phase diagram of the Hybrid situation for (a) non-LPL (CPL or EPL) with $\phi \neq 0, \pi$ and (b) LPL at $\phi = 0, \pi$.

Either the static symmetry-breaking perturbation term or the dynamic Floquet polarization light is able to open an energy gap and break TRS. However, the former is primarily dependent upon the parameter m (19) but instead the latter dictates the topological symmetry properties via polarization angle ϕ (24). It is therefore motivates us to study their concomitant effects on driving topological phase transitions.

In the regime where the intensity of polarization light dominates over the perturbation term with $A_0 \gg m$, the Berry curvature is qualitatively consistent with those of Floquet mode presented in Figs. 5-6 and thus not shown hereby. Accordingly, the topological properties are again dictated by the polarization angle ϕ and the Chern numbers can be summarized as follows

$$C = \begin{cases} \pm \text{sgn}(\phi), & \phi \neq 0, \pi \\ 0, & \phi = 0, \pi, \end{cases} \quad (27)$$

which manifestly reflect the polarization-controlled topology. In comparison, the static perturbation term governs the behavior of Berry curvature when the light intensity is comparable to or smaller than the perturbative mass ($A_0 \leq m$). Under this circumstance, the structural parameters t_x and t_z replace the polarization angle ϕ to determine the Chern number as $C = \pm \text{sgn}(t_x t_z)$. This indicates the topological phase transition is dictated solely by the microscopic struc-

tural parameters t_x and t_z . Fig. 8 schematically summarizes the central conclusions for the Hybrid situation.

IV. Anomalous Hall conductivity

Subsequently, we are going to examine the behavior of quantum transport accompanied by the topological phase transition. The anomalous Hall conductivity (AHC) [40, 82–87] represents a fundamental signature of momentum-space topology, stemming from the geometric Berry curvature $\Omega_z(\mathbf{k})$ intrinsic to the electronic band structure. Distinct from conventional Hall effects [88], which require external magnetic fields (ordinary Hall effect) or Landau-level quantization (quantum Hall effect) [89], the AHC originates solely from the momentum-space Berry phase accumulation in crystalline materials [1, 16]. It is therefore expected to emerge a finite transverse conductivity σ_{xy} in our models at zero external field, serving as an experimental signature of symmetry-protected topological phases.

The transverse AHC is formally expressed as [40, 82–84, 87]

$$\sigma_{xy} = \frac{e^2}{\hbar} \sum_n \int_{\text{BZ}} \frac{d^2 \mathbf{k}}{(2\pi)^2} f(E^n(\mathbf{k})) \Omega_z^n(\mathbf{k}), \quad (28)$$

where the summation n spans all energy bands, the integration covers the Brillouin zone (BZ), and $\Omega_z^n(\mathbf{k})$ denotes the Berry curvature of the n -th band. Hereby, the Fermi-Dirac distribution is given by

$$f(E) = \frac{1}{1 + e^{(E-E_f)/k_B T}}, \quad (29)$$

with E_f defining the Fermi energy. At the zero-temperature limit ($T \rightarrow 0$), the $f(E)$ reduces to a step function,

$$f(E(\mathbf{k})) \rightarrow \Theta(E(\mathbf{k}) - E_f), \quad (30)$$

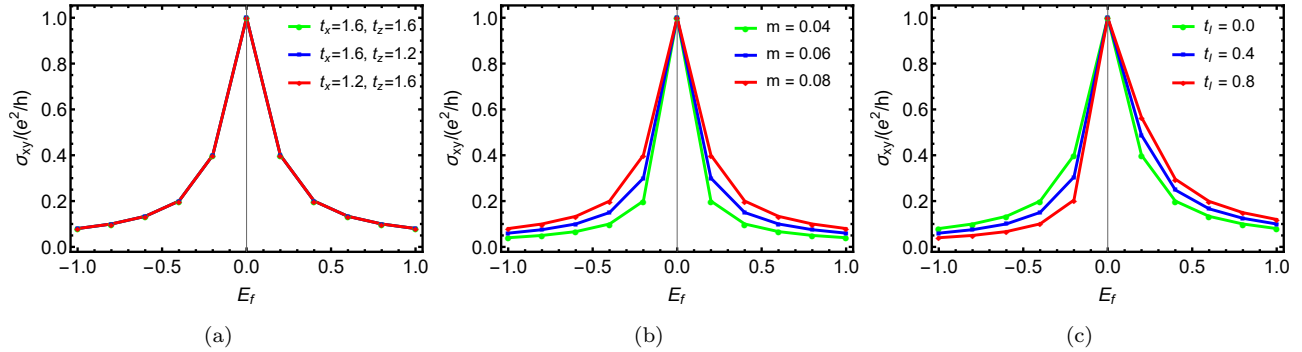


FIG. 9. (Color online) The E_f -dependent AHC $\sigma_{xy}/(e^2/\hbar)$ of the perturbative model for (a) $m = 0.08$ and $t_I = 0.0$ with variations of t_x , t_z , (b) $t_x = t_z = 1.6$, $m = 0.08$ with $t_I \neq 0$, and (c) $t_x = t_z = 1.6$, $t_I = 0.0$ with distinct values of m .

effectively restricting the integration to states below E_f . Generally, the AHC becomes quantized at temperatures where thermal excitations are negligible ($k_B T \ll \Delta_{\text{gap}}$). In the following, let us systematically analyze the behavior of AHC for the models introduced in Sec. II.

We commence with studying the perturbative model in Sec. II B 1. Following Eq. (28) and assuming the equilibrium-state $f(E)$, the numerical results in Fig. 9 present the Fermi level E_f dependence of the AHC. It clearly shows that the AHC saturates to the quantized value at $E_f = 0$, $\sigma_{xy} = \frac{C e^2}{h}$, $C = 1$, which is well consistent with the Thouless-Kohmoto-Nightingale-den Nijs (TKNN) formula [16]. For $E_f \neq 0$, σ_{xy} may be also sensitive to other parameters. As the parameter determines the PH symmetry and m adjusts the energy gap of the system, they provide a quantitative impact on the AHC as depicted in Fig. 9(a) and Fig. 9(b), respectively. In particular, $t_I \neq 0$ can break particle-hole (PH) symmetry, inducing an asymmetric AHC on distinct sides of $E_f = 0$ and the AHC is proportional to m . However, the parameters t_x , t_z shown in Fig. 9(c) only energy band symmetry but do not alter the magnitude of AHC.

Next, we move to consider the AHC of the Floquet model II B 2, which is characterized by the polarization angle and strength of external light as well as microscopic structural parameters. As aforementioned in Sec. III B, the nontrivial the Berry curvature and the Chern number are primarily determined by the polarization angle of external light. We therefore begin with investigating the influence of ϕ on the AHC as presented in

Fig. 10. Reading from Fig. 10(a), the LPL with $\phi = 0$, π generates negligible Berry curvature ($\Omega_z(\mathbf{k}) \approx 0$) across the Brillouin zone, yielding $\sigma_{xy} \rightarrow 0$ and preserving the topologically trivial insulating phase. In comparison, for either CPL ($\phi = \pm\pi/2$) or EPL ($\phi \neq 0, \pi, \pm\pi/2$) can induce non-zero Berry curvature with TRSB and drive a quantized AHC $\sigma_{xy} = e^2/h$ that is consistent with the behavior of Chern insulator when approaching the Fermi energy E_f . This indicates that the polarization-dependent symmetry breaking plays an essential role in switching trivial and topological insulating phases.

Given the qualitative similarity between CPL and EPL responses, let us subsequently take the CPL as an example to investigate the effects of other parameters on AHC. The strength of external field A_0 significantly modifies the energy gap despite it cannot qualitatively alter the Berry curvature. This establishes a positive correlation as shown in Fig. 10(b), where increasing A_0 enhances the AHC near the Fermi energy. Learning from Fig. 10(c), one can find that a finite t_I breaks PH symmetry and induces an asymmetric AHC about $E_f = 0$ with the asymmetry amplitude proportional to $|t_I|$. In contrast, t_x and t_z exhibit more complex influences as depicted in Fig. 10(d). They not only govern rotational symmetry but also quantitatively determine both the magnitude of energy gap, which jointly quantitatively modifying the AHC.

Furthermore, let us briefly comment on the AHC of the hybrid situation. In such case, the perturbation parameter m competes with the Floquet driving field A_0 . When A_0 is dominant at $A_0 \gg m$, the AHC exhibits

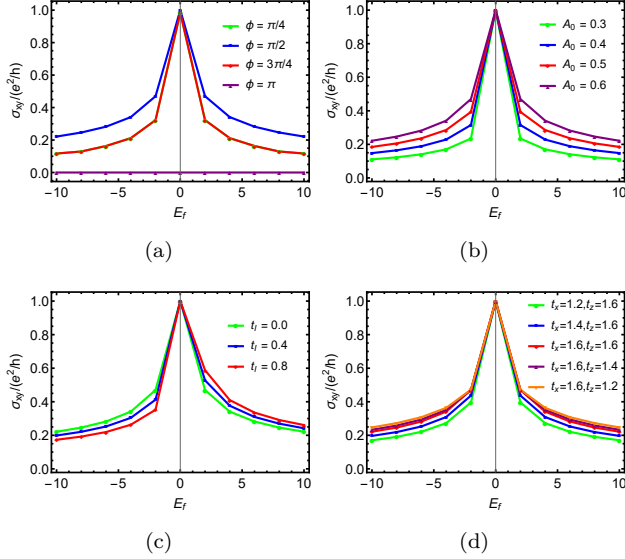


FIG. 10. (Color online) The E_f -dependent AHC $\sigma_{xy}/(e^2/\hbar)$ of the perturbative model for (a) distinct values of ϕ with $t_x = t_z = 1.6$, $A_0 = 0.6$, $\hbar\omega = 0.43$ at $t_I = 0.0$, (b) distinct values of A_0 with $t_x = t_z = 1.6$, $\phi = \pi/2$, $\hbar\omega = 0.43$ at $t_I = 0.0$, (c) $\phi = \pi/2$, $t_x = t_z = 1.6$, $A_0 = 0.6$, $\hbar\omega = 0.43$ with variations of a finite t_I , and (d) distinct values of t_x , t_z with $\phi = \pi/2$, $A_0 = 0.6$, $\hbar\omega = 0.43$ at $t_I = 0.0$.

analogous behavior to those shown in Fig. 10. Conversely, while m dominates over light-induced effects, the AHC behavior is restored to those of the perturbative model presented in Fig. 9.

To recapitulate, the AHC serves as a hallmark of topological states, arising from TRSB and nontrivial Berry curvature. We analyze two distinct gap-opening mechanisms, both of which break TRSB and thus generate nontrivial Chern number, yielding the quantized AHC. The key conclusions are provided in Fig. 9 and Fig. 10, which reveal universal scalings of magnitude and symmetry for the AHC near E_f with variations of interaction parameters.

V. Summary

In summary, we conduct a systematic investigation of nontrivial topological states emerging in 2D QBCP semimetals by introducing two complementary models: the static perturbative and the dynamic Floquet models, both designed to break TRS [40, 44, 60–68]. The de-

tailed analysis reveals that they produce different distributions of Berry curvature in momentum space. These accordingly give rise to nontrivial topological states and then induce distinct topological phase transitions via tuning their related parameters.

As for the static perturbative model, it eliminates the QBCP and opens an energy gap with the TRSB. The Berry curvature displayed in Fig. 3 exhibits symmetric under momentum inversion ($\mathbf{k} \rightarrow -\mathbf{k}$), leading to the emergence of Chern insulator characterized by Chern number $C = \pm \text{sgn}(t_x t_z)$ that is dependent on structural parameters t_x and t_z . Fig. 4 schematically presents how continuous variation of these coupling parameters drives discrete transitions between topologically distinct states.

Considering the Floquet model, the optical polarization angle (ϕ) plays an essential role in governing both the symmetry properties and topological character of Berry curvature as demonstrated in Fig. 6. As depicted in Fig. 5, the LPL at $\phi = 0$ or π preserves the central antisymmetry of the Berry curvature, resulting in a topologically trivial phase with Chern number. Conversely, either CPL or EPL breaks this antisymmetry of Berry curvature, yielding $\Omega_z(\mathbf{k}) \neq -\Omega_z(-\mathbf{k})$ shown in Fig. 6. This results in a nontrivial Chern insulator with Chern numbers $C = \pm \text{sgn}(\phi)$, where $\phi > 0$ and $\phi < 0$ correspond to RHPL and LHPL, respectively. This indicates that ϕ displayed in Fig. 7 acts as a tunable parameter to drive transitions between trivial and Chern insulator. For the sake of completeness, the competition between these two models is also briefly discussed and summarized in Fig. 8.

To proceed, we examine the behavior of AHC accompanied by the topological phase transitions at zero temperature [82–84, 87]. Due to the TRSB and nontrivial Berry curvature for both of two models, AHC exhibits universal quantization $\sigma_{xy} = C e^2/\hbar$ with $C = 1$ at $E_f = 0$. This is in well agreement with the TKNN formula [3, 16]. While $E_f \neq 0$, the magnitude of σ_{xy} displays parameter-dependent variations as collected in Fig. 9 and Fig. 10 for the perturbative and the dynamic Floquet models, respectively.

These results establish a tunable topological phase

transition from a QBCP semimetal to Chern insulator in the 2D QBCP materials. We hope that it would be helpful to provide a useful clue for experimental realization of dynamically controlled topological states in 2D semimetals.

ACKNOWLEDGEMENTS

We thank Wen Liu for the helpful discussions. J.W. was partially supported by the National Natural Science Foundation of China under Grant No. 11504360.

A. Derivation of the Floquet Hamiltonian

We hereby present the derivation of the Floquet Hamiltonian (15) in the main text. Expanding the full Hamiltonian (14) yields [65]

$$\mathcal{H}_F(\mathbf{k}) = \sum_{n=0}^{\infty} \mathcal{H}_F^{(n)}(\mathbf{k}). \quad (\text{A1})$$

Following the Ref. [40], we keep the series to the first order,

$$\mathcal{H}_F(\mathbf{k}) \sim \mathcal{H}_F^{(0)} + \mathcal{H}_F^{(1)}, \quad (\text{A2})$$

where the zero-order term is obtained by time-averaging [40, 65]:

$$\mathcal{H}_F^{(0)} = \frac{1}{T} \int_0^T dt \mathcal{H}(\mathbf{k}, t)$$

$$m_{\text{eff}} = \frac{eA_0 t_x t_z}{4\omega \hbar} \left\{ 8e^2 A_0^2 [1 + \cos(2\phi)] k_y + 20eA_0 \sin \phi k_x^2 + 12eA_0 \sin \phi k_y^2 + 4eA_0 \sin(2\phi) k_x k_y - 16e^2 A_0^2 \cos \phi k_x + 16(\cos \phi k_x - k_y) \mathbf{k}^2 + e^3 A_0^3 [3 \sin \phi + \sin(3\phi)] \right\}. \quad (\text{A11})$$

After combining \mathcal{H}_F^0 (A3) and \mathcal{H}_F^1 (A10), the final effective Floquet Hamiltonian is then left with

$$\mathcal{H}_F(\mathbf{k}) = t_I (e^2 A_0^2 + \mathbf{k}^2) \sigma_0 + \mathbf{d}(\mathbf{k}) \cdot \boldsymbol{\sigma}, \quad (\text{A12})$$

$$= \mathcal{H}_0(\mathbf{k}) + t_I e^2 A_0^2 \sigma_0 + t_x e^2 A_0^2 \cos \phi \sigma_1, \quad (\text{A3})$$

and the first order term is written as

$$\mathcal{H}_F^{(1)} = \frac{1}{2iT\hbar} \int_0^T dt_1 \int_0^{t_1} dt_2 [\mathcal{H}(\mathbf{k}, t_1), \mathcal{H}(\mathbf{k}, t_2)], \quad (\text{A4})$$

where the middle bracket denotes $[a, b] = ab - ba$.

After several calculations, Eq. (A2) can be reformulated as follows

$$\mathcal{H}(\mathbf{k}, t) \equiv F_0(\mathbf{k}, t) \sigma_0 + F_1(\mathbf{k}, t) \sigma_1 + F_3(\mathbf{k}, t) \sigma_3, \quad (\text{A5})$$

where

$$F_0(\mathbf{k}, t) \equiv t_I \mathbf{k}^2 + H_1(t), \quad (\text{A6})$$

$$F_1(\mathbf{k}, t) \equiv 2t_x k_x k_y + H_2(t), \quad (\text{A7})$$

$$F_3(\mathbf{k}, t) \equiv t_z (k_x^2 - k_y^2) + H_3(t). \quad (\text{A8})$$

This leads to

$$\begin{aligned} & [\mathcal{H}(\mathbf{k}, t_1), \mathcal{H}(\mathbf{k}, t_2)] \\ &= 2i[F_3(\mathbf{k}, t_1)F_1(\mathbf{k}, t_2) - F_1(\mathbf{k}, t_1)F_3(\mathbf{k}, t_2)]\sigma_2, \end{aligned} \quad (\text{A9})$$

and the first-order term can be represented by an effective mass,

$$\mathcal{H}_F^{(1)} = m_{\text{eff}} \sigma_2, \quad (\text{A10})$$

where the effective mass is designated as

where the vector \mathbf{d} is denominated as

$$\mathbf{d}(\mathbf{k}) = (t_x e^2 A_0^2 \cos \phi + 2t_x k_x k_y, m_{\text{eff}}, t_z (k_x^2 - k_y^2)). \quad (\text{A13})$$

[1] F. D. M. Haldane, *Phys. Rev. Lett.* **61**, 2015 (1988).

[2] C. L. Kane and E. J. Mele, *Phys. Rev. Lett.* **95**, 146802

- (2005).
- [3] M. Z. Hasan and C. L. Kane, *Rev. Mod. Phys.* **82**, 3045 (2010).
- [4] D. Xiao, M.-C. Chang, and Q. Niu, *Rev. Mod. Phys.* **82**, 1959 (2010).
- [5] X.-L. Qi and S.-C. Zhang, *Rev. Mod. Phys.* **83**, 1057 (2011).
- [6] W. X. Feng and Y. G. Yao, *Sci. China Phys. Mech. Astron.* **55**, 2199[C2212] (2012).
- [7] C.-K. Chiu, J. C. Y. Teo, A. P. Schnyder, and S. Ryu, *Rev. Mod. Phys.* **88**, 035005 (2016).
- [8] B. Yan and S.-C. Zhang, *Rep. Prog. Phys.* **75** 096501 (2012).
- [9] Yoichi Ando, *J. Phys. Soc. Jpn.* **82**, 102001 (2013).
- [10] J. H. Bardarson and J. E. Moore, *Rep. Prog. Phys.* **76** 056501 (2013).
- [11] C. W. J. Beenakker, *Annu. Rev. Condens. Matter Phys.* **4**, 113 (2013).
- [12] H. Zhang and S.-C. Zhang, *Phys. Status Solidi RRL* **7**, 72 (2013).
- [13] A. Bansil, H. Lin, and T. Das, *Rev. Mod. Phys.* **88**, 021004 (2016).
- [14] J. Lapano, *et al*, *Phys. Rev. Materials* **4**, 111201(R) (2020).
- [15] B. A. Bernevig, T. L. Hughes, and S. C. Zhang, *Science* **314**, 1757 (2006).
- [16] D. J. Thouless, M. Kohmoto, M. P. Nightingale, and M. den Nijs, *Phys. Rev. Lett.* **49**, 405 (1982).
- [17] R. Chen, C.-Z. Chen, J.-H. Gao, B. Zhou, and D.-H. Xu, *Phys. Rev. Lett.* **124**, 036803 (2020).
- [18] Z.-G. Chen, W. Zhu, Y. Tan, L. Wang, and G. Ma, *Phys. Rev. X* **11**, 011016 (2021).
- [19] Y. Bai, X. Zou, Z. Chen, R. Li, Bo Yuan, Y. Dai, B. Huang, and C. Niu, *ACS Nano*, 19, 9, 9265[C9272] (2025).
- [20] Z.-C. Xiang *et al.*, *Nat Commun* **14**, 5433 (2023).
- [21] H. Lu, H.-Q. Wu, B.-B. Chen, and Z. Y. Meng, *Phys. Rev. Lett.* **134**, 076601 (2025).
- [22] B. Wang, J. Yu, P. Sharma, and C.-C. Liu, *arXiv:2504.11177 [cond-mat.mes-hall]* (2025).
- [23] Y. He, S.H. Simon, and S.A. Parameswaran, *arXiv:2505.06354 [cond-mat.str-el]* (2025).
- [24] P. Emanuel, A. Keselman, and Y. Oreg, *arXiv:2505.07950 [cond-mat.str-el]* (2025).
- [25] Z. Lin, W. Yang, H. Lu, D. Zhai, and W. Yao, *arXiv:2505.09009 [cond-mat.mes-hall]* (2025).
- [26] C.-Z. Chang *et al.*, *Science* **340**, 167-170 (2013).
- [27] Y. Huang, Y. Fu, P. Zhang, K. L. Wang, and Q. L. He, *J. Phys.: Condens. Matter* **36** 37LT01 (2024).
- [28] X. Zhang, G. Pan, B.-B. Chen, H. Li, K. Sun, and Z. Y. Meng, *Phys. Rev. B* **107**, L241105 (2023).
- [29] Z. Ji, H. Park, M. E. Barber, C. Hu, K. Watanabe, T. Taniguchi, J.-H. Chu, X. Xu, and Z.-X. Shen, *Nature* **635**, 578[C583] (2024).
- [30] L.-X. Lei *et al*, *Chinese Phys. Lett.* **41** 090301 (2024).
- [31] A. H. Castro Neto, F. Guinea, N. M. R. Peres, K. S. Novoselov, and A. K. Geim, *Rev. Mod. Phys.* **81**, 109 (2009).
- [32] H.-Z. Lu, W.-Y. Shan, W. Yao, Q. Niu, and S.-Q. Shen, *Phys. Rev. B* **81**, 115407 (2010).
- [33] S.-Q. Shen, W.-Y. Shan, and H.-Z. Lu, *SPIN* 01:01, 33-44 (2011).
- [34] K. Taguchi, D. Oshima, Y. Yamaguchi, T. Hashimoto, Y. Tanaka, and M. Sato, *Phys. Rev. B* **101**, 235201 (2020).
- [35] V. Vargiamidis, P. Vasilopoulos, and N. Neophytou, *arXiv:2212.10667 [cond-mat.mes-hall]* (2022).
- [36] H. Lu, S. Sur, S.-S. Gong, and D. N. Sheng, *Phys. Rev. B* **106**, 205105 (2022).
- [37] Z.-M. Wang, R. Wang, J.-H. Sun, T.-Y. Chen, and D.-H. Xu, *Phys. Rev. B* **107**, L121407 (2023).
- [38] Y. Mo, X. Wang, Z.-Y. Zhuang, and Z. Yan, *arXiv:2411.10851 [cond-mat.mes-hall]* (2024).
- [39] H. Huang, Z. Liu, H. Zhang, W. Duan, and D. Vanderbilt, *Phys. Rev. B* **92**, 161115(R) (2015).
- [40] K. Saha, *Phys. Rev. B* **94**, 081103(R) (2016).
- [41] S. Mondal and S. Basu, *Phys. Rev. B* **105**, 235441 (2022).
- [42] Q. Chen, L. Du, and G. A. Fiete, *Phys. Rev. B* **97**, 035422 (2018).
- [43] Y. Zhang, Y.-W. Tan, H. L. Stormer, and P. Kim, *Nature* **438**, 201[C204] (2005).
- [44] Y. D. Chong, X.-G. Wen, and M. Soljacic, *Phys. Rev. B* **77**, 235125 (2008).
- [45] K. Sun and E. Fradkin, *Phys. Rev. B* **78**, 245122 (2008).
- [46] K. Sun, H. Yao, E. Fradkin, and S. A. Kivelson, *Phys. Rev. Lett.* **103**, 046811 (2009).
- [47] J. M. Murray and O. Vafek, *Phys. Rev. B* **89**, 201110(R) (2014).
- [48] M.-R. Li, A.-L. He, and H. Yao, *Phys. Rev. Research* **4**, 043151 (2022).
- [49] Y.-S. Fu and J. Wang, *Annals of Physics* **470**, 169811 (2024).
- [50] R. Liquito, M. Goncalves, and E. V. Castro, *Phys. Rev. B* **109**, 174202 (2024).
- [51] X. Wan, S. Sarkar, S.-Z. Lin, and K. Sun, *Phys. Rev.*

- Lett.* **130**, 216401 (2023).
- [52] X. Ji, J. Gao, C. Yue, Z. Wang, H. Wu, X. Dai, and H. Weng, *Phys. Rev. B* **106**, 235103 (2022).
- [53] N. Sobrosa, M. Goncalves, and E. V. Castro, *Phys. Rev. B* **109**, 184206 (2024).
- [54] J. Jung, H. Lim, and B.-J. Yang, [arXiv:2307.12528 \[cond-mat.mes-hall\]](https://arxiv.org/abs/2307.12528) (2023).
- [55] D. Wu, Y. Huang, S. Sun, J. Gao, Z. Guo, H. Weng, Z. Fang, K. Jiang, and Z. Wang, *Sci. China Phys. Mech. Astron.* **65**, 256811 (2022).
- [56] J. Wang, C. Ortix, J. van den Brink, and D. V. Efremov, *Phys. Rev. B* **96**, 201104(R) (2017).
- [57] Y.-M. Dong, Y.-H. Zhai, D.-X. Zheng, and J. Wang, *Phys. Rev. B* **102**, 134204 (2020).
- [58] S. Ray, M. Vojta, and L. Janssen, *Phys. Rev. B* **98**, 245128 (2018).
- [59] H. Pan, M. Wu, Yl Liu, and S. A. Yang, *Sci. Rep.* **5**, 14639 (2015).
- [60] T. Oka and H. Aoki, *Phys. Rev. B* **79**, 081406(R) (2009).
- [61] M. S. Rudner and N. H. Lindner, *Nat Rev Phys* **2**, 229[C244 (2020).
- [62] P. Liu, C. Cui, L. Li, R. Li, D.-H. Xu, and Z.-M. Yu, [arXiv:2503.19614 \[cond-mat.str-el\]](https://arxiv.org/abs/2503.19614) (2025).
- [63] P.-H. Fu, S. Mondal, J.-F. Liu, Y. Tanaka, and J. Cayao, [arXiv:2505.20205 \[cond-mat.supr-con\]](https://arxiv.org/abs/2505.20205) (2025).
- [64] T. Yokoyama, [arXiv:2505.10332 \[cond-mat.supr-con\]](https://arxiv.org/abs/2505.10332) (2025).
- [65] M. Bukov, L. D'Alessio, and A. Polkovnikov, *Advances in Physics*, **64**, 2, 139-226 (2015).
- [66] O. Benhaida, E. H. Saidi, L. B. Drissi, and R. Ahl Laamara, [arXiv:2412.17763 \[cond-mat.mes-hall\]](https://arxiv.org/abs/2412.17763) (2024).
- [67] O. V. Kibis, M. V. Boev, I. V. Iorsh, and V. M. Kovalev, *J. Phys.: Condens. Matter* **37**, 035503 (2025).
- [68] S. Sajad Dabiri and Reza Asgari, [arXiv:2503.12620 \[cond-mat.mtrl-sci\]](https://arxiv.org/abs/2503.12620) (2025).
- [69] Y.-H. Zhai and J. Wang, *Nucl. Phys. B* **966** (2021) 115371.
- [70] S. Y. Zhou, G.-H. Gweon, A. V. Fedorov, P. N. First, W. A. de Heer, D.-H. Lee, F. Guinea, A. H. Castro Neto, and A. Lanzara, *Nature Mater* **6**, 770[C775 (2007).
- [71] C.-H. Bao, H.-Y. Zhang, T. Zhang, X. Wu, L.-P. Luo, S.-H. Zhou, Q. Li, Y.-H. Hou, W. Yao *et al.* *Phys. Rev. Lett.* **126**, 206804 (2021).
- [72] Z. Wang, J.-S. Yan, K.-X. Chen, and S.-S. Lyu, *Phys. Rev. B* **111**, 085425 (2025).
- [73] Z. F. Wang, Z. Liu, and F. Liu, *Phys. Rev. Lett.* **110**, 196801 (2013).
- [74] H.-Q. Wu, Y.-Y. He, C. Fang, Z. Y. Meng, and Z.-Y. Lu, *Phys. Rev. Lett.* **117**, 066403 (2016).
- [75] F. Ma, J. Feng, F. Li, Y. Wu, and D. Zhou, [arXiv:2412.00619 \[cond-mat.mtrl-sci\]](https://arxiv.org/abs/2412.00619) (2024).
- [76] Z. Jalali-Mola and O. Hess, [arXiv:2503.17263 \[physics.optics\]](https://arxiv.org/abs/2503.17263) (2025).
- [77] C. Li, *et al.*, [arXiv:2505.01767 \[cond-mat.mes-hall\]](https://arxiv.org/abs/2505.01767) (2025).
- [78] P. G. de Oliveira and A. S. T. Pires, [arXiv:2407.20296 \[cond-mat.mes-hall\]](https://arxiv.org/abs/2407.20296) (2024).
- [79] H.-B. Kim, T. Yuk, and S.-J. Sin, [arXiv:2407.21098 \[cond-mat.mes-hall\]](https://arxiv.org/abs/2407.21098) (2024).
- [80] A. Mukherjee and B. Singh, [arXiv:2410.04515 \[cond-mat.mes-hall\]](https://arxiv.org/abs/2410.04515) (2024).
- [81] J. O. A. Biscocho and K. H. A. Villegas, [arXiv:2410.14213 \[cond-mat.supr-con\]](https://arxiv.org/abs/2410.14213) (2024).
- [82] X.-L. Qi, Y.-S. Wu, and S.-C. Zhang, *Phys. Rev. B* **74**, 085308 (2006).
- [83] S. Pradhan, K. Samanta, and A. K. Nandy, [arXiv:2412.02324 \[cond-mat.mtrl-sci\]](https://arxiv.org/abs/2412.02324) (2024).
- [84] T. Habe, *Phys. Rev. B* **111**, 035303 (2025).
- [85] R. Karplus and J. M. Luttinger, *Phys. Rev.* **95**, 1154 (1954).
- [86] P. Středa, *Phys. Rev. B* **82**, 045115 (2010).
- [87] S. Thakur and S. Baidya, [arXiv:2501.11025 \[cond-mat.mtrl-sci\]](https://arxiv.org/abs/2501.11025) (2025).
- [88] E. H. Hall, *American Journal of Mathematics*, 2(3): 287-292 (1879).
- [89] K. v. Klitzing, *Rev. Mod. Phys.* **58**, 519 (1986).